

# Disk2Planet: A Robust and Automated Machine Learning Tool for Parameter Inference in Disk-Planet Systems

SHUNYUAN MAO (毛顺元),<sup>1</sup> RUOBING DONG (董若冰),<sup>2,3</sup> KWANG MOO YI,<sup>4</sup> LU LU,<sup>5</sup> SIFAN WANG,<sup>6,7</sup> AND PARIS PERDIKARIS<sup>8</sup>

<sup>1</sup>*Department of Physics and Astronomy, University of Victoria, Victoria, BC V8P 5C2, Canada, symao@uvic.ca*

<sup>2</sup>*Department of Physics and Astronomy, University of Victoria, Victoria, BC V8P 5C2, Canada*

<sup>3</sup>*Kavli Institute for Astronomy and Astrophysics, Peking University, Beijing 100871, People's Republic of China, rbdong@pku.edu.cn*

<sup>4</sup>*Department of Computer Science, University of British Columbia, Vancouver, BC V6T 1Z4, Canada*

<sup>5</sup>*Department of Statistics and Data Science, Yale University, New Haven, CT 06511, USA*

<sup>6</sup>*Graduate Group in Applied Mathematics and Computational Science, University of Pennsylvania, Philadelphia, PA 19104, USA*

<sup>7</sup>*Institute for Foundations of Data Science, Yale University, New Haven, CT 06520, USA*

<sup>8</sup>*Department of Mechanical Engineering and Applied Mechanics, University of Pennsylvania, Philadelphia, PA 19104, USA*

## ABSTRACT

We introduce Disk2Planet, a machine learning-based tool to infer key parameters in disk-planet systems from observed protoplanetary disk structures. Disk2Planet takes as input the disk structures in the form of two-dimensional density and velocity maps, and outputs disk and planet properties, that is, the Shakura–Sunyaev viscosity, the disk aspect ratio, the planet–star mass ratio, and the planet’s radius and azimuth. We integrate the Covariance Matrix Adaptation Evolution Strategy (CMA–ES), an evolutionary algorithm tailored for complex optimization problems, and the Protoplanetary Disk Operator Network (PPDONet), a neural network designed to predict solutions of disk–planet interactions. Our tool is fully automated and can retrieve parameters in one system in three minutes on an Nvidia A100 graphics processing unit. We empirically demonstrate that our tool achieves percent-level or higher accuracy, and is able to handle missing data and unknown levels of noise.

*Keywords:* Protoplanetary disks (1300) – Planetary-disk interactions (2204) – Hydrodynamical simulations (767) – Neural networks (1933) – Open source software (1866)

## 1. INTRODUCTION

Planets form in protoplanetary disks: flattened, gaseous disks surrounding newborn stars (Andrews 2020). To study planet formation in the outer disk beyond the snowline, a straightforward approach is to directly image the forming planets in these disks (e.g., Keppler et al. 2018; Müller et al. 2018; Wagner et al. 2018; Christiaens et al. 2019; Haffert et al. 2019; Hashimoto et al. 2020; Wang et al. 2020; Currie et al. 2022; Zhou et al. 2022; Wagner et al. 2023). Successful detections can provide critical information about the process, such as the mass and orbit of the forming planets. However, this approach is challenging with current observational techniques as the signals from the stars and disks overwhelm those from the planets (Currie et al. 2022). These factors severely limit our understanding of how planets form.

To detect young planets embedded in protoplanetary disks, an alternative method is to infer their presence

and constrain their parameters from observations of large-scale disk structures produced by disk-planet interactions (Paardekooper et al. 2022). The morphology of these structures, such as gaps (e.g., Paardekooper & Mellema 2006; Rosotti et al. 2016; Dipierro & Laibe 2017), spiral arms (e.g., Bae & Zhu 2018; Dong et al. 2015a), vortices (e.g., Zhu et al. 2014), and kinematic perturbations (e.g., Pinte et al. 2018; Teague et al. 2018; Izquierdo et al. 2021; Rabago & Zhu 2021), depends on the properties of the disk and the planets, such as the viscosity and aspect ratio of the disk, and the masses and orbits of the planets.

Deriving planetary parameters from observed disk structures requires solving *the inverse problem*: deducing causes from observed effects. It involves fitting observations with parametrized disk-planet models predicted by a *forward problem solver*, a solver that calculates the effects from the causes. The process iteratively fine-tunes parameters to fit the observed data.

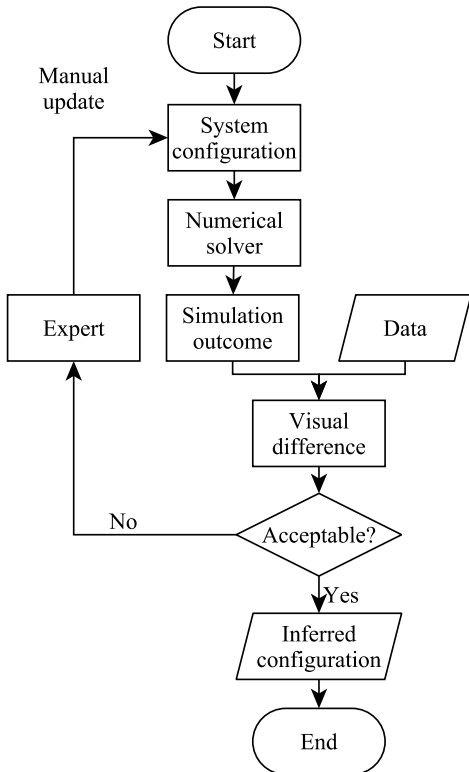


**Figure 1.** The framework of conventional inverse problem solvers. Each iteration begins with an estimation of the system configuration, which includes parameters in a disk-planet system. This configuration is sent to a numerical solver to generate the resulting disk maps. Expert analysis then evaluates the visual discrepancies between the simulation outcomes and the observational data, leading to iterative refinements of the system parameters.

Conventional inverse problem solvers, as illustrated in Fig. 1, are both computationally and labor-wise intensive. The forward problem solver relies on numerical simulations, each demanding substantial computational resources (e.g., Cilibrasi et al. 2023). This demand is multiplied by the number of iterations needed to process a single observed system (e.g., Dipierro et al. 2015; Dong et al. 2015b; Jin et al. 2016; Pinte et al. 2019). Additionally, because of the expensive computing, to make the most out of each run, the procedure requires significant expert involvement for the initial setup, continuous monitoring, and adjustments of simulations. As the discovery of structures in disks accelerates—with over 100 disks newly resolved in a regular year (Benisty et al. 2022)—the demand to fit all disk observations through simulations vastly outstrips the available computational and human resources.

Naturally, alternative approaches that aim to reduce computation has been explored, such as those that directly map planet-induced structures to parameters in

disk-planet systems without numerical simulations. Initially, this mapping involved using empirical formulas to analytically correlate a small number of (or a single) scalar observable metrics of disk structures, such as gap width or depth, to system parameters (e.g., Dong et al. 2018; Zhang et al. 2018; Dong & Fung 2017). Recently, the same correlations are learnt by neural networks (Auddy & Lin 2020; Auddy et al. 2022) instead. However, all such approaches rely solely on a limited number of scalar metrics, failing to encapsulate the rich information in images, resulting in degeneracies and large uncertainties in the results (e.g., Fung et al. 2014).

To address these limitations, Convolutional Neural Networks (CNNs) (O’Shea & Nash 2015; Li et al. 2021) are employed in several pioneering works to map entire images to disk and planet parameters (Auddy et al. 2021; Zhang et al. 2022; Terry et al. 2022; Ruzza et al. 2024). The CNNs establish the relationships between disk density maps or synthetic observations (“effects”) and system parameters (“causes”) by training on simulated data where both are known. These networks analyze spatial correlations among pixel values to identify the characteristics of planet-induced disk structures, leveraging the comprehensive information in an image rather than relying on a limited array of highly synthesized scalar metrics (e.g., gap width). This method not only improves inference accuracy but also streamlines the process of retrieving planet parameters from disk observations for end users by (1) obviating the need for numerical simulations and (2) circumventing the tedious iterative fitting process.

However, the accuracy of parameters retrieved by CNN-based inverse problem solvers typically only reaches the order of 0.1. Furthermore, such accuracy is assured solely for images within the training data distribution and may significantly deteriorate when applied to real observations, which may not conform to this distribution. This is particularly evident with images (1) with noise (Ruzza et al. 2024, §5.3), as the noise level in actual observations is measured only afterward and varies from one observation to another, challenging the preparation of the training dataset; and (2) with missing parts, e.g., due to foreground absorption (Bruderer et al. 2014, Fig. 1; Tsukagoshi et al. 2019). These scenarios underscore the inherent difficulties in applying CNN-based solvers to real observations.

Given the traditional methods (e.g., Fig. 1) are computationally and labor-wise expensive, and the CNN-based solvers are limited in accuracy and robustness, a better approach is needed. We address these issues by developing a fast, and fully automated inverse problem solver, named Disk2Planet, that can infer planet and

disk parameters from observed disk structures with unprecedented accuracy and robustness. It replaces cumbersome simulations with PPDONet (Mao et al. 2023), a fast machine learning-based solver capable of predicting one system in approximately 0.01 seconds on an Nvidia A100 chip. In addition, Disk2Planet is the first in the field of planet formation to utilize CMA-ES (Hansen & Ostermeier 1996, 1997, 2001; Hansen et al. 2003; Hansen 2006; Hansen et al. 2019) for iterative parameter updates, automating the parameter inference process and eliminating the need for human intervention.

Disk2Planet can process one system with a single image input in just three minutes on an Nvidia A100 GPU. It achieves accuracy on the order of 0.001 to 0.01 in inferred parameters for the first time. Additionally, Disk2Planet is capable of handling images with unknown noise levels, missing parts of arbitrary shapes, and various combinations of density and/or velocities, demonstrating its robustness in real observations.

## 2. METHOD

The inputs for our inverse problem solver consist of one or a combination of 2D maps of surface density and velocity distributions in a steady-state disk with a planet on a stable circular orbit. The solver is designed to find the optimal set of five parameters—Shakura–Sunyaev viscosity ( $\alpha$ ), disk aspect ratio ( $h_0$ ), planet–star mass ratio ( $q$ ), and planetary location (radius  $r_p$  and azimuth  $\theta_p$ )—that results in the minimal differences between the predicted disk model and the input data. This is accomplished through an iterative process outlined in Fig. 2.

In each iteration, we use a 5D Gaussian distribution to represent our current knowledge of ( $\alpha$ ,  $h_0$ ,  $q$ ,  $r_p$ ,  $\theta_p$ ). The mean of the Gaussian indicates the most probable parameter values. Initially, we sample 4,096 parameter sets uniformly in the parameter space of interest:  $3 \times 10^{-4} \leq \alpha \leq 0.1$ ,  $0.05 \leq h_0 \leq 0.1$ ,  $5 \times 10^{-5} \leq q \leq 2 \times 10^{-3}$ , and  $r_p$  and  $\theta_p$  within the input data image’s boundaries (50–150 au for  $r_p$  and  $2\pi$  for  $\theta_p$ , or wherever the truncation due to cropping is; §3.4). The mean of the Gaussian is initialized to the parameters with the lowest score (§2.2) among the 4,096 parameter sets. The standard deviation of the Gaussian reflects the confidence in the estimate and is initially set to 0.01<sup>1</sup>. Each iteration includes four steps:

1. Sample 128 sets of parameters from the Gaussian distribution;

2. Predict the disk model for each parameter set using the forward problem solver PPDONet (§2.1);
3. Assign a score to each prediction to quantify how well it matches the input data (§2.2);
4. Update the Gaussian distribution’s mean and standard deviation based on the scores using the Covariance Matrix Adaptation Evolution Strategy (CMA-ES; §2.3).

The iterative process is repeated until the score in step (3) can no longer be minimized, indicating that the best possible set of parameters has been found.

Figure 2 illustrates how the tool works. The input data (panel (a)) contains a surface density map generated using the FARGO3D code (Masset 2000; Benítez-Llambay & Masset 2016) with its true parameters listed on the side. The evolution of the score is shown in panel (b). The inferred (optimal) parameters are shown in panel (c), where we achieve sub-percentage level accuracy for all five parameters. Panel (c) also shows the surface density map corresponding to the inferred parameters, obtained using PPDONet, enabling visual inspection.

### 2.1. The PPDONet-based Forward Problem Solver

To infer parameters automatically and accurately, our method tests many sets of parameters per iteration (e.g., 128 sets in our experiments) instead of a single set as in traditional approaches. This necessitates a fast forward problem solver, as traditional simulations are too slow to frequently test parameter sets. We employ PPDONet, the only public fast forward problem solver at the time of writing.

For each set of ( $\alpha$ ,  $h_0$ ,  $q$ ) sampled during iterations, PPDONet (Mao et al. 2023) predicts surface density  $\Sigma$ , radial velocity  $v_r$ , and azimuthal velocity  $v_\theta$  maps, each computed in 0.01 second on an Nvidia A100 chip. Line-of-sight velocity maps  $v_{\text{LOS}} = v_r \cos(\theta) - v_\theta \sin(\theta)$  can be synthesized in post-processing. These maps are then rotated and stretched according to the planet location ( $r_p$ ,  $\theta_p$ ) in the current sample. PPDONet is a publicly available machine learning tool<sup>2</sup> that efficiently maps scalar parameters from partial differential equations to their solutions. As demonstrated in Mao et al. (2023, Fig. 2), the predicted disk maps are visually indistinguishable from FARGO3D simulations within the parameter space of interest defined earlier.

### 2.2. The Score for Data-Output Comparisons

<sup>1</sup> See the instructions at [https://CMA--ES.github.io/cmaes-sourcecode\\_page.html](https://CMA--ES.github.io/cmaes-sourcecode_page.html).

<sup>2</sup> <https://github.com/smao-astro/PPDONet>

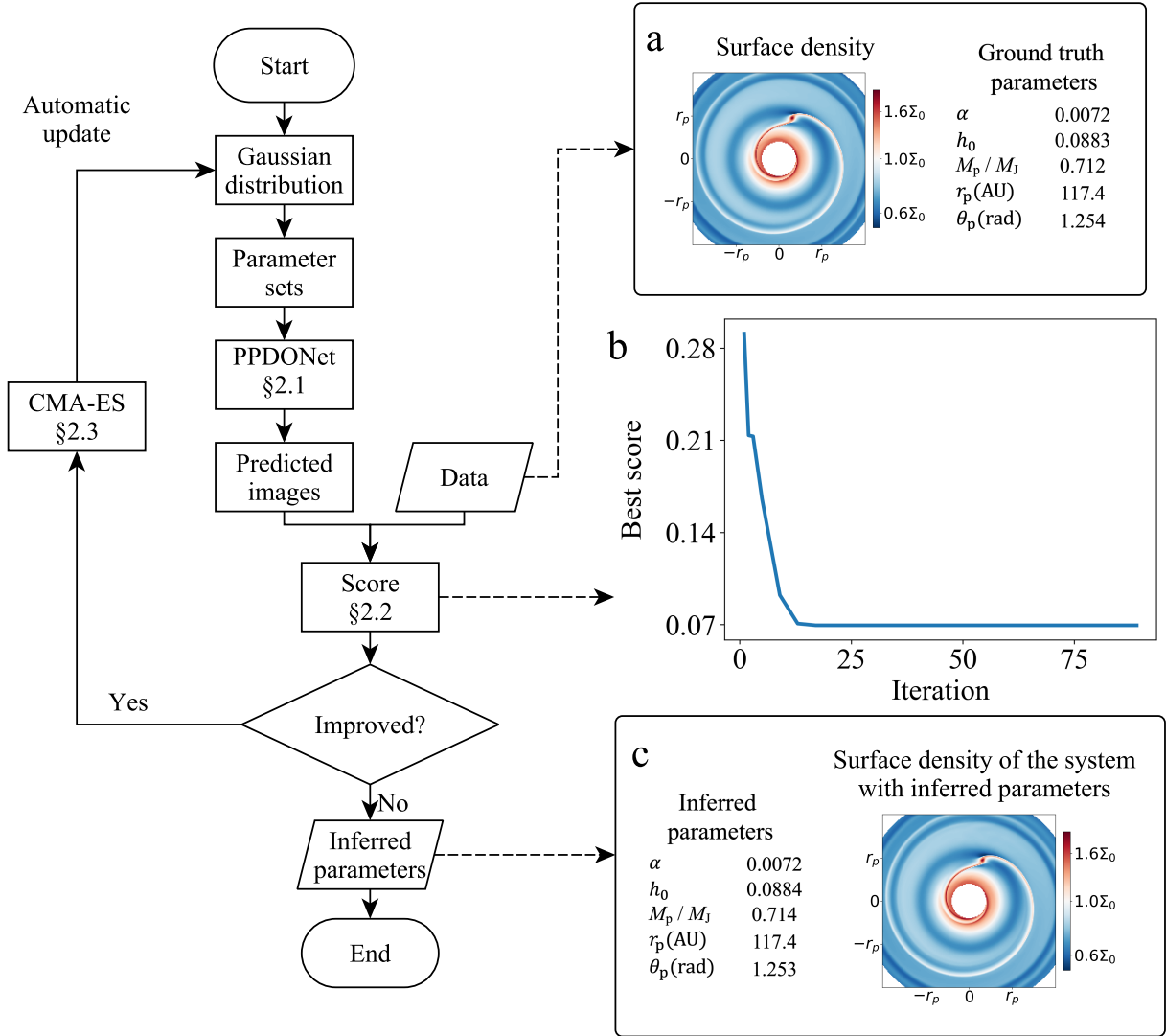


**Figure 2.** A flow chart illustrating the iterative parameter update procedure in Disk2Planet inverse problem solver. The solver iterates a 5D Gaussian distribution representing the most probable parameters ( $\alpha$ ,  $h_0$ ,  $q$ ,  $r_p$ ,  $\theta_p$ ) that result in the minimal difference between the model and the input data. At each iteration, the Gaussian distribution is refined by testing 128 sets of parameters sampled from the current distribution. These parameters are processed by the ML-based solver PPDONet (§2.1) to predict the corresponding disk maps. Differences between these maps and the data are quantified by the score (§2.2). The CMA-ES optimizer (§2.3) updates the Gaussian distribution to converge towards parameter sets with smaller scores. This process iterates until the distribution converges to the optimal parameters. On the right, we show an example of the inference process: (a) the input surface density map and its true parameters; (b) the evolution of the best score over iterations; (c) the inferred parameters and the corresponding surface density solution.

The PPDONet-predicted disk map for each sampled parameter set is compared with the corresponding input data to generate a score quantifying their differences. We opt for the L2 error metric over the structural similarity index measure (SSIM) (Wang et al. 2004) due to its simplicity. In addition, our tests show that using L2 and SSIM as the evaluation metric yield similar results. For velocities, the score is the relative  $L_2$  error:

$$L_2(\text{velocity}) = \|\text{pred} - \text{data}\|_2 / \|\text{data}\|_2, \quad (1)$$

where  $\|\cdot\|_2$  denotes the root mean square over all pixel values. For surface density, the score is the logarithmic relative  $L_2$  error (e.g. Zhang et al. 2022)

$$L_2(\Sigma) = \|\log_{10} \text{pred} - \log_{10} \text{data}\|_2 / \|\log_{10} \text{data}\|_2. \quad (2)$$

The score is designed to handle the data complications illustrated in Fig. 3. For noisy data (block A),  $L_2$  is directly computed between the noisy data and the noise-free predicted model. For data with missing parts (block B), the error calculation is confined to valid pixels

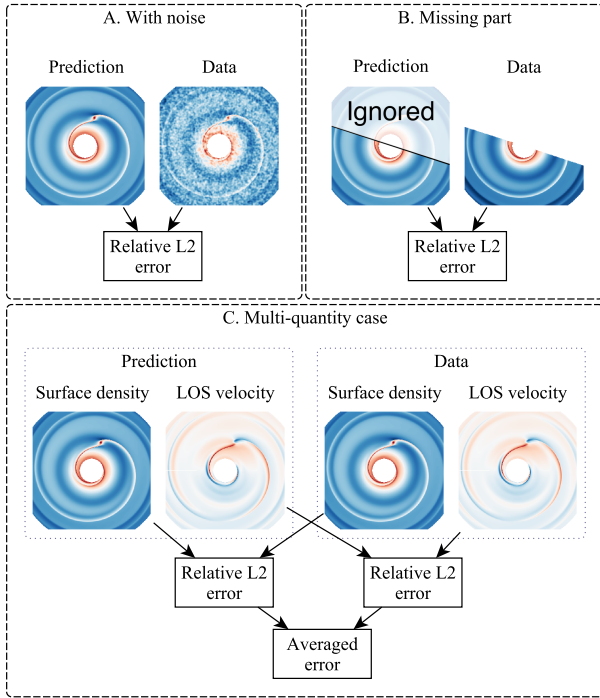


**Figure 3.** Score calculation for three cases of input data. Block A: For noisy input data, the score is calculated the same way as for noise-free data. Block B: For input data with missing areas, only the available pixels are used. Block C: For input data containing multiple quantities, the error for each quantity is calculated, and then the average of all errors is taken as the score.

only. If the data includes multiple components, such as  $\Sigma$  and  $v_{\text{LOS}}$  (block C),  $L_2$  for each component are averaged to produce a composite measure. The score is not designed to account for effects caused by disk inclination, which is often known for individual systems (e.g., Huang et al. 2018, Table 1), enabling deprojection of the input data prior to parameter inferences when the observations probe the disk midplane (e.g., millimeter dust continuum emission).

### 2.3. The Optimization Algorithm CMA-ES

We use an optimization algorithm to iterate parameter updates based on their corresponding scores. In optimization problems, there are two primary classes of algorithms: gradient-based and gradient-free. Gradient-based methods typically offer superior performance; however, they are unsuitable for our problem because the derivatives of scores with respect to parameters are unavailable. Consequently, we rely on a gradient-free technique: the Covariance Matrix Adaptation Evolution Strategy (CMA-ES) (Hansen & Ostermeier 1996, 1997, 2001; Hansen et al. 2003; Hansen 2006). CMA-ES is renowned for its superior performance on benchmark problems (Hansen et al. 2010; García et al. 2009) where

the correlation between parameters and scores is complex and not well understood analytically.

CMA-ES automatically updates the mean and covariance matrix of the Gaussian distribution to minimize the scores (§2.2) of the parameters sampled from the Gaussian distribution over iterations. Each update in CMA-ES follows an adaptive strategy similar to that found in evolutionary biology: The algorithm ranks parameter sets by their scores, selecting the lowest half as “parents”. It then blends these parent sets through recombination and mutation to calculate the mean and covariance matrix for the new Gaussian distribution. This new Gaussian reflects the most successful parameter combinations at that moment, guiding the search towards promising directions. The updated Gaussian is then employed to generate “children” parameter sets for the next iteration. This iterative process repeats until the score improvement plateaus, indicating that the optimal parameters have been effectively identified by the latest Gaussian distribution.

## 3. PERFORMANCE

In this section, we evaluate the parameter inference accuracy of Disk2Planet. We begin with the baseline case in which the input data contains a complete noise-free map of surface density (§3.1). We then test cases in which the input data contains multiple physical quantities (§3.2), noises (§3.3), and missing parts (§3.4).

### 3.1. The baseline case — input data with surface density only

Fig. 4 shows the inferred versus ground truth planet masses for 256 tests uniformly sampled from the parameter space specified in Mao et al. (2023, Table 1). Overall, the two agree well. The agreement can be quantitatively assessed using the  $r_2$ -score:

$$r_2 = 1 - SS(M_p^{\text{inferred}} - M_p^{\text{true}}) / SS(M_p^{\text{true}} - \overline{M_p^{\text{true}}}), \quad (3)$$

where  $SS$  denotes the sum of square of all cases and  $\overline{M_p^{\text{true}}}$  is the mean of all ground truth values. An  $r_2$ -score close to one indicates near-perfect agreement. Our tool achieves an  $r_2$ -score of 0.9994. For comparison, Bayesian network-based parameter inference achieves  $r_2$ -scores of 0.82 (Auddy et al. 2022, Fig. 3), and CNN-based parameter inference typically achieves  $r_2$ -scores of 0.97 to 0.98 (Auddy et al. 2021, Fig. 4; Ruzza et al. 2024, Fig. 5).

Another metric for assessing the tool’s performance is the error distribution of each parameter, as done by Zhang et al. (2022) and Ruzza et al. (2024). In each test, we quantify the error in each inferred parameter



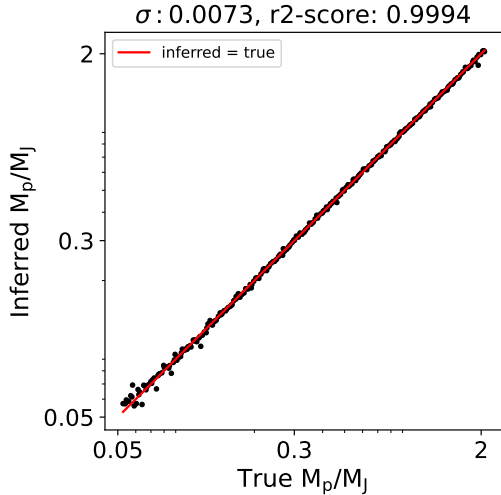


**Figure 4.** Ground truth and inferred planet masses in 256 tests using full noise-free maps of surface density as input. The tests achieve an  $r_2$ -score (Eq. 3) of 0.9994 and an inference uncertainty  $\sigma$  of 0.0073, indicating near-perfect agreement (red solid line). See §3.1 for details.

as:

$$\text{Err}(\alpha) = \log_{10}(\alpha^{\text{inferred}}) - \log_{10}(\alpha^{\text{true}}), \quad (4a)$$

$$\text{Err}(h_0) = (h_0^{\text{inferred}} - h_0^{\text{true}})/h_0^{\text{true}}, \quad (4b)$$

$$\text{Err}(q) = \log_{10}(q^{\text{inferred}}) - \log_{10}(q^{\text{true}}), \quad (4c)$$

$$\text{Err}(r_p) = (r_p^{\text{inferred}} - r_p^{\text{true}})/r_p^{\text{true}}, \quad (4d)$$

$$\text{Err}(\theta_p) = \theta_p^{\text{inferred}} - \theta_p^{\text{true}}. \quad (4e)$$

The errors for  $\alpha$  and  $q$  are calculated on a logarithmic scale due to their wide range across several orders of magnitude (Ruzza et al. 2024, Eq. 13). The errors for  $h_0$  and  $r_p$  are normalized. We then define the inference uncertainty  $\sigma$  as half the difference between the error distribution’s 84<sup>th</sup> and 16<sup>th</sup> percentiles, and list them in the first column in Fig. 5:  $\sigma(\alpha) = 0.022$ ,  $\sigma(h_0) = 0.0015$ ,  $\sigma(q) = 0.0073$ ,  $\sigma(r_p) = 0.00047$ ,  $\sigma(\theta_p) = 0.0018$ . In comparison, CNN-based parameter inference achieves  $\sigma(q) = 0.16$  (Zhang et al. 2022) and 0.13 (Ruzza et al. 2024), and  $\sigma(\alpha) = 0.23$  (Zhang et al. 2022).

We examine the error distributions and possible correlations in the multi-dimensional parameter space in Fig. 6a. The histograms on the diagonal show the distributions of individual parameters while the off-diagonal panels highlight pairwise correlations. Notably, all distributions are centered, indicating little systematic bias in the inferred parameters. Additionally, only two pairwise correlations (out of a total of  $C(5, 2) = 10$ ) are not isotropic:  $\text{Err}(\alpha)$  vs  $\text{Err}(q)$  exhibits a positive correlation, echoing Zhang et al. (2022, Fig. 5), while  $\text{Err}(r_p)$  is negatively correlated with  $\text{Err}(\theta_p)$ .

### 3.2. Input data with multiple quantities

Disk2Planet can incorporate surface density  $\Sigma$ , radial velocity  $v_r$ , and azimuthal velocity  $v_\theta$  in any combination. For example, we can supply two maps,  $\Sigma + v_{\text{LOS}}$ , as illustrated in Fig. 5 (case (b)). This scenario mimics real situations where gas line emission observations (e.g., Zhang et al. 2021) provide these quantities. As the amount of information in the input data increases, the parameter inference accuracy improves, resulting in smaller errors. Compared to the baseline case (a), adding  $v_{\text{LOS}}$  reduces uncertainties for the five inferred parameters by 3% to 47% in 256 tests. Additionally, supplying three maps,  $\Sigma + v_r + v_\theta$ , as input data (case c) further reduces uncertainties since  $v_r + v_\theta$  provide more information than  $v_{\text{LOS}}$ .

### 3.3. Input data with noise

Observational data often contain noise. Our inverse problem solver can handle noisy input data, as shown in cases (d) and (e) in Fig. 5. They are created by introducing random uniform noises in  $\Sigma$  (case (d)) and  $\Sigma + v_{\text{LOS}}$  (case (e)). The noises have a spatial scale of 2.5 AU (Zhang et al. 2018, §2.3; equivalent to 0.018 arcsec at 140 pc), added to the logarithmic pixel values with a standard deviation  $0.6\times$  the average of the quantity. The resulting uncertainties for the five parameters in both cases are 2 – 4 $\times$  those in the corresponding noise-free inputs (cases (a) and (b)). The associated multi-dimensional error distributions are shown in Fig. 6b, with trends similar to those in the baseline case (Fig. 6a; §3.1).

### 3.4. Input data with missing parts

In observations, signals in certain regions may be missing or masked for various reasons, such as foreground extinction (Bruderer et al. 2014; Tsukagoshi et al. 2019). Figure 5 illustrates two such cases: the  $\Sigma$  map is cropped radially beyond  $1.1r_p$  (f) and azimuthally in half (g; the planet is in the cropped region). In both scenarios, the tool performs parameter inference in all 256 tests, albeit with uncertainties 1 – 9 $\times$  those in the baseline case with a full  $\Sigma$  map (a). This is expected, as cropping reduces the amount of information in the input image. In the radial cropping case,  $\sigma(h_0)$  and  $\sigma(r_p)$  have the largest increases (4.3 $\times$  and 6.0 $\times$ , respectively), although their absolute values remain low (0.007 and 0.003, respectively). In the azimuthal cropping case, a 9-fold increase in  $\sigma(\theta_p)$  stands out among the five uncertainties, attributed to the loss of substructures near the planet, crucial for its accurate localization. The absolute value of  $\sigma(\theta_p)$ , 0.016 ( $1^\circ$ , or 1.6 AU for a planet at 100 AU), remains smaller than the typical resolution achieved in to-

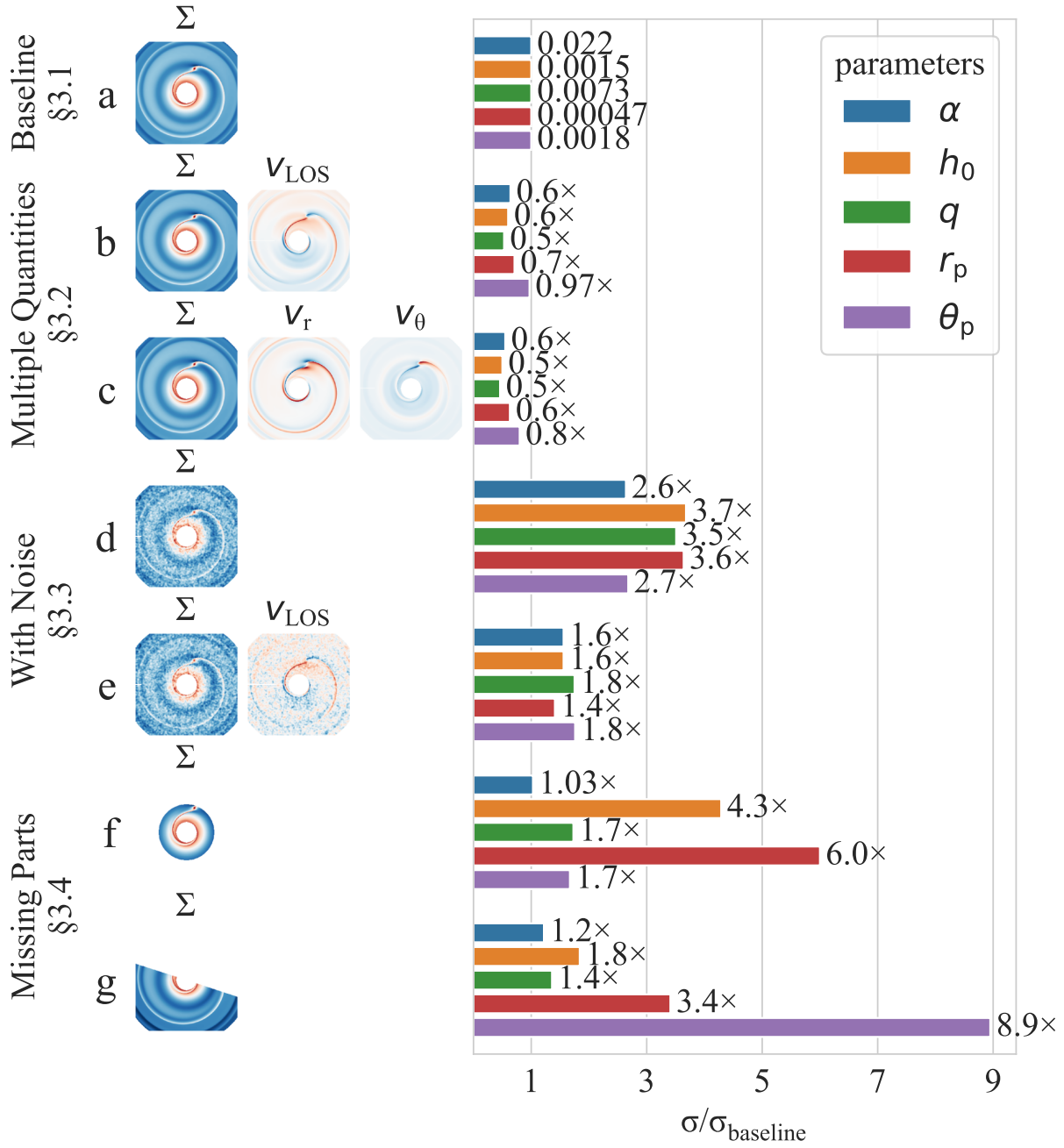


**Figure 5.** Representative examples of the input datasets, and the corresponding parameter inference uncertainties ( $\sigma$ ). The input datasets contain images of, from top to bottom,  $\Sigma$  (a),  $\Sigma+v_{\text{LOS}}$  (b),  $\Sigma+v_r+v_\theta$  (c),  $\Sigma$  with noise (d),  $\Sigma+v_{\text{LOS}}$  with noise (e), radially cropped  $\Sigma$  (f), and azimuthally cropped  $\Sigma$  (g). 256 tests are run for each. The uncertainties are calculated as half the difference between the error distribution's 84<sup>th</sup> and 16<sup>th</sup> percentiles. The numbers on the bar plot represent the uncertainties for the baseline dataset (a), and how the uncertainties in the other datasets (b)–(g) compared to those in the baseline case.

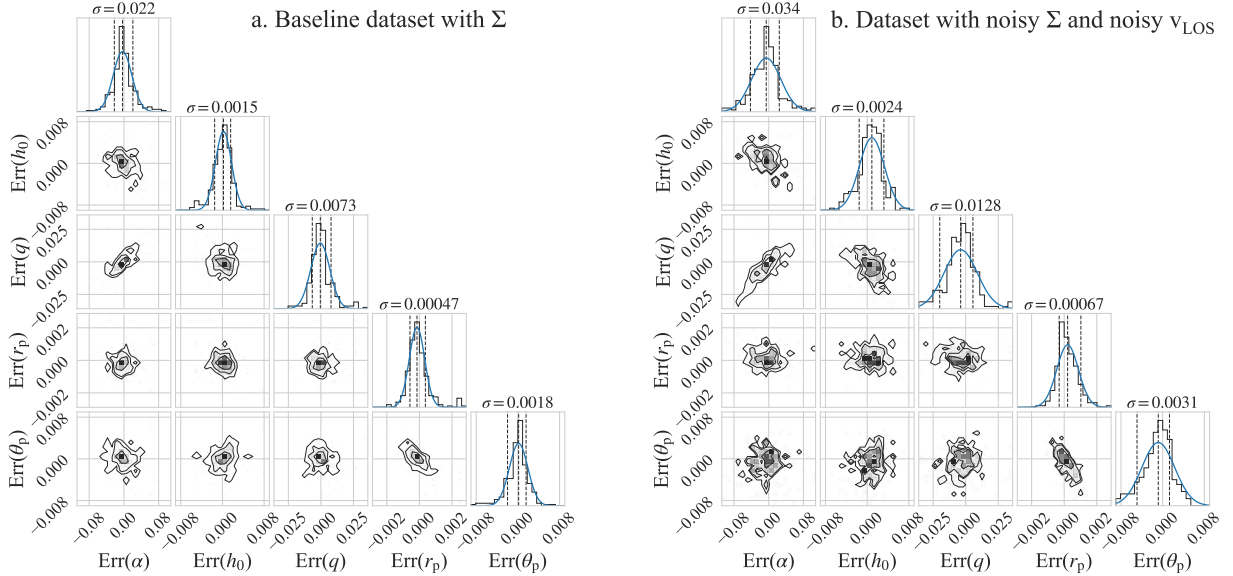


**Figure 6.** Corner plots showing the distribution of errors in the inferred parameters (Eq. 4). Corresponding panels on the two sides are on the same scales. The histograms on the diagonal show the distributions of individual parameters, while the off-diagonal panels highlight pairwise correlations. See §3.1 for details.

day’s high-resolution imaging observations of disks (e.g., Benisty et al. 2022).

#### 4. ADVANTAGES OVER EXISTING INVERSE PROBLEM SOLVERS

Disk2Planet is robust against noisy data (3.3). This is because our optimization focuses on large-scale disk morphology (e.g., spiral arms, gap), more than noises (usually small-scale). To demonstrate this, imagine a small error in the inferred disk scale height. This will cause noticeable differences in the spiral arm pitch angle (Fung & Dong 2015), which is much more than the influence of the noise (§2.2). Thus Disk2Planet is generally noise-robust. In contrast, CNN-based methods (Auddy et al. 2021; Zhang et al. 2022; Ruzza et al. 2024) rely on *local* spatial patterns, thus are more prone to noises. They result in significantly larger errors when the signal-to-noise ratio is below ten (e.g., a planet mass error of 0.68 dex versus 0.13 dex; Ruzza et al. 2024, §5.3).

Our inverse problem solver can process incomplete images with missing parts in arbitrary shapes in a straightforward manner. As illustrated in Fig. 3 (Block B), the missing parts are ignored and do not contribute to the parameter inference. In contrast, CNN-based methods require completed images, as every pixel contributes to the convolution, which is key to CNNs in extracting information. In theory, CNNs can also be trained with datasets that have the same missing parts as the real observations. However, this is impractical in real-life applications, because it is often difficult to predict which

parts of the image will be missing in real observations, and the missing parts can vary between observations.

Our inverse problem solver works with input images of any spatial resolution since the entire procedure is resolution-independent. In contrast, CNN-based solvers are often trained on datasets with fixed resolutions. To minimize training costs, low resolutions are typically used, such as  $64 \times 64$  in Zhang et al. (2022) or  $128 \times 128$  in Ruzza et al. (2024), which can degrade detailed disk substructures like spiral arms. Additionally, due to limitations in the training sets, CNN-based tools can only operate properly when the input images have the same resolution as the training sets; if not, regridding is needed, which may result in a loss of information.

Disk2Planet locates planets by matching their induced substructures with those in the data. This contrasts with CNN-based approaches (e.g., Ruzza et al. 2024), which requires users to provide prior knowledge of the planet’s location. Augmenting the training dataset in PPDONet to accommodate different planet locations is not needed neither, in contrast to CNN-based approach (e.g. Zhang et al. 2022).

Disk2Planet has an advantage over the more traditional CNN-based methods when dealing with input images with parameters outside the specified range. Our method leverages the fast forward solver, PPDONet, which generates a modelled image (Fig. 2, panel (c)) based on the inferred parameters at no additional computational cost. This feature enables users to visually compare the modelled image with the input image. When the input image parameters fall outside the



specified range, the inferred parameters are constrained within the predefined parameter space by our tool, thus lead the modelled image differs from the input image. Consequently, visual comparison provides an intuitive means of verifying results and identifying potential issues with input data. In comparison, CNN-based approach doesn't offer a straightforward approach to visually verify the results.

## 5. CONCLUSIONS AND FUTURE PERSPECTIVES

We have developed a fast and fully automated inverse problem solver, Disk2Planet, capable of inferring five parameters — the Shakura–Sunyaev viscosity ( $\alpha$ ), disk aspect ratio ( $h_0$ ), planet–star mass ratio ( $q$ ), and the planet's radius and azimuth — from 2D steady-state disk-planet systems. Inferring these parameters from surface density in one system takes three GPU minutes on an Nvidia A100 machine. Our solver requires minimal human intervention and is user-friendly for newcomers without prior experience in numerical simulations of disk–planet interactions.

The architecture of the solver and an example application are shown in Fig. 2. The solver is built on the machine learning tool PPDONet, which predicts the disk maps created by a planet (Mao et al. 2023). The solver employs the evolutionary optimization algorithm CMA–ES (Hansen & Ostermeier 1996, 1997, 2001; Hansen et al. 2003; Hansen 2006; Hansen et al. 2019), which samples parameters from a 5D Gaussian distribution in each iteration and refines the distribution by minimizing the difference between the model and the input data.

The inputs to the solver consist of 2D maps of gas surface density and velocities in a disk. The solver can handle data with unknown noise levels, incomplete data with missing parts, and user-defined combinations of quantities (Fig. 5). It achieves percentage-level or smaller errors in the inferred parameters in the tests performed in this work (Fig. 4), representing at least an order of magnitude improvement over previous tools based on Convolutional Neural Networks (e.g., Auddy et al. 2021; Zhang et al. 2022; Ruzza et al. 2024). As expected, the errors decrease as more information is provided by the input data.

The current version of Disk2Planet may be improved in certain ways. First, it is designed to work with 2D

maps of gas surface density and velocities derived from observations (e.g., Zhang et al. 2021), rather than directly with observational data. To extend its functionality to disk observations directly, an updated PPDONet capable of directly predicting synthetic images is required. Training such a network would necessitate a dataset generated from gas+dust simulations and synthetic observations, and sampling additional parameters such as dust properties and planet masses and orbits for multi-planet systems. Once such a dataset is available, future work can readily adapt our approach to update the existing inverse problem solver. These modifications would require minimal changes to the existing PPDONet architecture and our inverse problem solver framework. Second, unlike Auddy et al. (2022) and Ruzza et al. (2024), it does not produce uncertainties on the inferred parameters. However, the forward problem solver employed, PPDONet, provides the predicted disk maps corresponding to the inferred parameters (Fig. 2). These disk maps can be visually compared to data, offering users a straightforward way to evaluate the quality of the inferences.

The data and source code for this work will be available at <https://github.com/smao-astro/Disk2Planet> upon publication.

1 We are grateful to an anonymous referee for constructive  
2 suggestions that improved our paper. We thank Jaehan  
3 Bae, Xuening Bai, Pablo Benítez-Llambay, Shengze Cai,  
4 Miles Cranmer, Bin Dong, Scott Field, Jeffrey Fung, Xi-  
5 aotian Gao, Jiequn Han, Pinghui Huang, Pengzhan Jin,  
6 Xiaowei Jin, Hui Li, Tie-Yan Liu, Zhiping Mao, Chris  
7 Ormel, Wenlei Shi, Karun Thanjavur, Yiwei Wang, Yin-  
8 hao Wu, Zhenghao Xu, Minhao Zhang, Wei Zhu for help  
9 and useful discussions in the project.

10 S.M. and R.D. are supported by the Natural Sciences  
11 and Engineering Research Council of Canada (NSERC)  
12 and the Alfred P. Sloan Foundation. S.M. and R.D. ac-  
13 knowledge the support of the Government of Canada's  
14 New Frontiers in Research Fund (NFRF), [NFRFE-  
15 2022-00159]. This research was enabled in part by  
16 support provided by the Digital Research Alliance of  
17 Canada [alliance.can.ca](http://alliance.can.ca).

## REFERENCES

- Andrews, S. M. 2020, *Annual Review of Astronomy and Astrophysics*, 58, 483
- Auddy, S., Dey, R., Lin, M.-K., Carrera, D., & Simon, J. B. 2022, *The Astrophysical Journal*, 936, 93
- Auddy, S., Dey, R., Lin, M.-K., & Hall, C. 2021, *The Astrophysical Journal*, 920, 3
- Auddy, S., & Lin, M.-K. 2020, *The Astrophysical Journal*, 900, 62

- Bae, J., & Zhu, Z. 2018, *The Astrophysical Journal*, 859, 118
- Benisty, M., Dominik, C., Follette, K., et al. 2022, arXiv preprint arXiv:2203.09991
- Benítez-Llambay, P., & Masset, F. S. 2016, *The Astrophysical Journal Supplement Series*, 223, 11
- Bruderer, S., van der Marel, N., Van Dishoeck, E. F., & van Kempen, T. A. 2014, *Astronomy & Astrophysics/Astronomie et Astrophysique*, 562
- Christiaens, V., Casassus, S., Absil, O., et al. 2019, *Monthly Notices of the Royal Astronomical Society*, 486, 5819
- Cilibrasi, M., Flock, M., & Szulágyi, J. 2023, *Monthly Notices of the Royal Astronomical Society*, 523, 2039
- Currie, T., Lawson, K., Schneider, G., et al. 2022, *Nature Astronomy*, 6, 751
- Dipierro, G., & Laibe, G. 2017, *Monthly Notices of the Royal Astronomical Society*, 469, 1932
- Dipierro, G., Price, D., Laibe, G., et al. 2015, *Monthly Notices of the Royal Astronomical Society: Letters*, 453, L73
- Dong, R., & Fung, J. 2017, *The Astrophysical Journal*, 835, 38
- Dong, R., Li, S., Chiang, E., & Li, H. 2018, *The Astrophysical Journal*, 866, 110
- Dong, R., Zhu, Z., Rafikov, R. R., & Stone, J. M. 2015a, *The Astrophysical Journal Letters*, 809, L5
- Dong, R., Zhu, Z., & Whitney, B. 2015b, *The Astrophysical Journal*, 809, 93
- Fung, J., & Dong, R. 2015, *The Astrophysical Journal Letters*, 815, L21
- Fung, J., Shi, J.-M., & Chiang, E. 2014, *The Astrophysical Journal*, 782, 88
- García, S., Molina, D., Lozano, M., & Herrera, F. 2009, *Journal of Heuristics*, 15, 617
- Haffert, S., Bohn, A., De Boer, J., et al. 2019, *Nature Astronomy*, 3, 749
- Hansen, N. 2006, *Towards a new evolutionary computation: Advances in the estimation of distribution algorithms*, 75
- Hansen, N., Akimoto, Y., & Baudis, P. 2019, *CMA-ES/pycma on Github, Zenodo*, DOI:10.5281/zenodo.2559634, doi: 10.5281/zenodo.2559634
- Hansen, N., Auger, A., Ros, R., Finck, S., & Pošík, P. 2010, in *Proceedings of the 12th annual conference companion on Genetic and evolutionary computation*, 1689–1696
- Hansen, N., Müller, S. D., & Koumoutsakos, P. 2003, *Evolutionary computation*, 11, 1
- Hansen, N., & Ostermeier, A. 1996, in *Proceedings of IEEE international conference on evolutionary computation*, IEEE, 312–317
- Hansen, N., & Ostermeier, A. 1997, *Eufit*, 97, 650
- . 2001, *Evolutionary computation*, 9, 159
- Hashimoto, J., Aoyama, Y., Konishi, M., et al. 2020, *The Astronomical Journal*, 159, 222
- Huang, J., Andrews, S. M., Dullemond, C. P., et al. 2018, *The Astrophysical Journal Letters*, 869, L42
- Izquierdo, A. F., Testi, L., Facchini, S., Rosotti, G. P., & van Dishoeck, E. F. 2021, arXiv preprint arXiv:2104.09596
- Jin, S., Li, S., Isella, A., Li, H., & Ji, J. 2016, *The Astrophysical Journal*, 818, 76
- Keppler, M., Benisty, M., Müller, A., et al. 2018, *Astronomy & Astrophysics*, 617, A44
- Li, Z., Liu, F., Yang, W., Peng, S., & Zhou, J. 2021, *IEEE transactions on neural networks and learning systems*
- Mao, S., Dong, R., Lu, L., et al. 2023, *The Astrophysical Journal Letters*, 950, L12
- Masset, F. 2000, *Astronomy and Astrophysics Supplement Series*, 141, 165
- Müller, A., Keppler, M., Henning, T., et al. 2018, *Astronomy & Astrophysics*, 617, L2
- O’Shea, K., & Nash, R. 2015, arXiv preprint arXiv:1511.08458
- Paardekooper, S.-J., Dong, R., Duffell, P., et al. 2022, arXiv preprint arXiv:2203.09595
- Paardekooper, S.-J., & Mellema, G. 2006, arXiv preprint astro-ph/0603132
- Pinte, C., Price, D., Ménard, F., et al. 2018, *The Astrophysical Journal Letters*, 860, L13
- Pinte, C., van Der Plas, G., Ménard, F., et al. 2019, *Nature Astronomy*, 3, 1109
- Rabago, I., & Zhu, Z. 2021, *Monthly Notices of the Royal Astronomical Society*, 502, 5325
- Rosotti, G. P., Juhasz, A., Booth, R. A., & Clarke, C. J. 2016, *Monthly Notices of the Royal Astronomical Society*, 459, 2790
- Ruzza, A., Lodato, G., & Rosotti, G. P. 2024, arXiv preprint arXiv:2402.12448
- Teague, R., Bae, J., Bergin, E. A., Birnstiel, T., & Foreman-Mackey, D. 2018, *The Astrophysical Journal Letters*, 860, L12
- Terry, J., Hall, C., Abreau, S., & Gleyzer, S. 2022, *The Astrophysical Journal*, 941, 192
- Tsukagoshi, T., Momose, M., Kitamura, Y., et al. 2019, *The Astrophysical Journal*, 871, 5
- Wagner, K., Follette, K. B., Close, L. M., et al. 2018, *The Astrophysical Journal Letters*, 863, L8
- Wagner, K., Stone, J., Skemer, A., et al. 2023, *Nature Astronomy*, 7, 1208

- Wang, J. J., Ginzburg, S., Ren, B., et al. 2020, The Astronomical Journal, 159, 263
- Wang, Z., Bovik, A. C., Sheikh, H. R., & Simoncelli, E. P. 2004, IEEE transactions on image processing, 13, 600
- Zhang, K., Booth, A. S., Law, C. J., et al. 2021, The Astrophysical Journal Supplement Series, 257, 5
- Zhang, S., Zhu, Z., & Kang, M. 2022, Monthly Notices of the Royal Astronomical Society, 510, 4473
- Zhang, S., Zhu, Z., Huang, J., et al. 2018, The Astrophysical Journal Letters, 869, L47
- Zhou, Y., Sanghi, A., Bowler, B. P., et al. 2022, The Astrophysical Journal Letters, 934, L13
- Zhu, Z., Stone, J. M., Rafikov, R. R., & Bai, X.-n. 2014, The Astrophysical Journal, 785, 122